JACS
JOURNAL OF THE AMERICAN CHEMICAL SOCIETY
Article
pubs.acs.org/JACS

Giant Stretchability and Reversibility of Tightly Wound Helical Carbon Nanotubes

Jianyang Wu,[†] Jianying He,[†] Gregory M. Odegard,[‡] Shijo Nagao,[†,§] Quanshui Zheng,[∥] and Zhiliang Zhang*[,†]

[†]NTNU Nanomechanical Lab, Norwegian University of Science and Technology (NTNU), Trondheim N-7491, Norway
[‡]Department of Mechanical Engineering, Michigan Technological University, 1400 Townsend Drive, Houghton, Michigan 49931-1295, United States
[§]The Institute of Scientific and Industrial Research, Osaka University, Mihogaoka 8-1, Ibaraki, Osaka 567-0047, Japan
[∥]Department of Engineering Mechanics and Center for Nano and Micro Mechanics, Tsinghua University, Beijing 100084, China

Supporting Information

ABSTRACT: There is a surging interest in 3D graphitic nanostructures which possess outstanding properties enabling them to be prime candidates for a new generation of nanodevices and energy-absorbing materials. Here we study the stretching instability and reversibility of tightly wound helical carbon nanotubes (HCNTs) by atomistic simulations. The intercoil van der Waals (vdW) interaction-induced flattening of HCNT walls prior to loading is constrained by the defects coordinated for the curvature formation of helices. The HCNTs exhibit extensive stretchability in the range from 400% to 1000% as a result of two distinct deformation mechanisms depending on the HCNT size. For small HCNTs tremendous deformation is achieved by domino-type partial fracture events, whereas for large HCNTs this is accomplished by stepwise buckling of coils. The formation and fracture of edge-closed graphene ribbons occur at lower temperatures, while at elevated temperatures the highly distributed fracture realizes a phenomenal stretchability. The results of cyclic stretching-reversing simulations of large HCNTs display pronounced hysteresis loops, which produce large energy dissipation via full recovery of buckling and vdW bondings. This study provides physical insights into the origins of high ductility and superior reversibility of hybrid CNT structures.

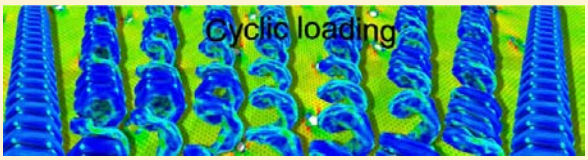

INTRODUCTION

The discovery of carbon nanotubes (CNTs)[1] has triggered intense study into these quasi-one-dimensional tubular structures made by rolling up graphene sheets into seamless cylinders. They exhibit a unique combination of superior electronic, thermal, and mechanical properties and are extremely lightweight, which inspires further efforts to exploit their promising properties in many different applications.[2,3] Mechanically, CNTs are the strongest and stiffest materials known to mankind, composed entirely of sp^2-bonded carbon atoms in the hexagonal network. The tensile strength and Young modulus of CNTs reported in the literature are almost in the range of 100−200 GPa and 1−2 TPa, respectively.[4−8] Mechanical failure of CNTs under a tensile load can proceed in two distinct patterns as either plastic deformation or fracture, depending on the temperature and curvature.[9] Specifically, when subjected to tension loading at high temperatures, CNTs with large diameters will undergo plastic deformation and can sustain extremely large plastic strains as a result of nucleation and kink-motion mechanisms.[10−12] Meanwhile, owing to their hollow tubular structure and large aspect ratio, they are prone to buckle when placed under various loading conditions such as axial compression, bending, and torsion and combinations of these loads.[13] Buckled CNTs with no atomic defects have the ability to completely recover after unloading.[14]

Helical CNTs (HCNTs), predicted and observed[15−18] shortly after the discovery of the straight CNTs, are another emerging form of carbon nanomaterials. Due to the combination of their helical morphology and the fantastic properties of CNTs, HCNTs hold great potential for a range of applications. For instance, the large surface area and high peroxidase-like activity of HCNTs enable them to be used as biocatalysts and biosensors.[19] For HCNT/polymer nanocomposites, the bonding strength and load transfer between HCNTs and the polymer matrix are greater than those found in CNT/polymer nanocomposites because of the mechanical interlocking of the coils and polymer.[20,21] Depending on the location of pentagon- and heptagon-based carbon ring structures, HCNTs can exhibit metallic or semiconducting electrical behaviors (similar to CNTs) and semimetallic characteristics which are not present in straight CNTs.[22] Electric currents flowing through HCNTs produce inductive magnetic fields, which enables them to be used as molecular nanosolenoids in nanoswitches and electromagnetic nanotransformers.[22,23] HCNTs are capable of emitting high-density, uniform, and stable electron fields, which suggests that they can be utilized for flat panel field emission displays.[24,25] In addition,

Received: May 1, 2013
Published: July 22, 2013

dx.doi.org/10.1021/ja404330q | J. Am. Chem. Soc. 2013, 135, 13775−13785

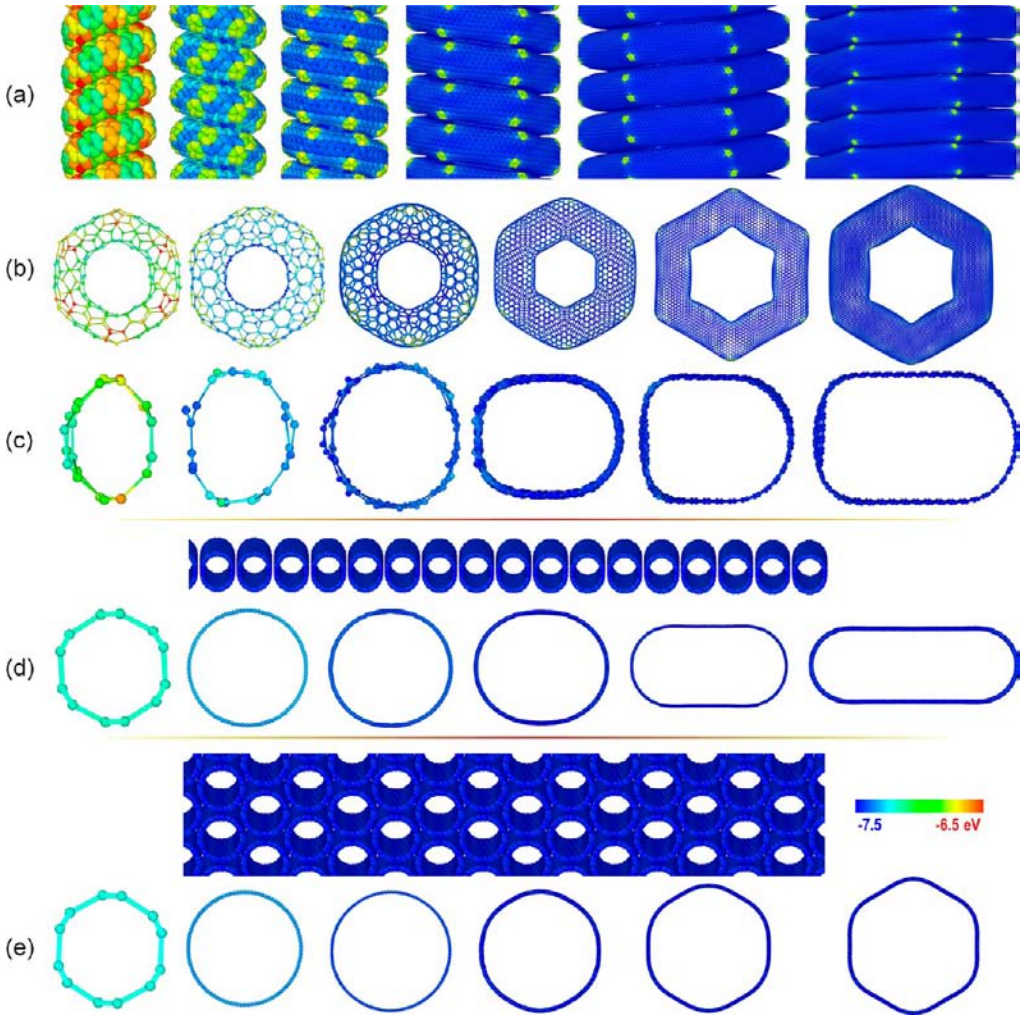

Figure 1. Atomic model motifs of HCNTs and the cross-section of different CNT bundles. (a) Side and (b) top views of equilibrated tightly wound HCNTs with four turns. The pentagon and heptagon rings are located at the inner and outward ridges of the HCNTs, respectively. (c) Side views of CNT coils of HCNTs. The flattening of HCNT halts at the vicinity of defects. The left part of the CNT cross-section corresponds to the "inside" of the coils. (d, e) Cross-sections of a perfect CNT in the equilibrium state where the tubes are packed in a parallel and triangular lattice arrangement, with an initial intertube spacing of 3.35 Å. For large-diameter CNTs, two distinct cross-sectional morphologies with racetrack-like and round-hexagonal shapes are observed for parallel and triangular lattice packing, respectively. Atoms are colored according to the potential energy, and the pentagon defects in the HCNTs are highlighted.

HCNT nanospring sensors are able to measure small forces and masses in the femtogram range.[26] Inspired by these important applications, great effort has been devoted to the study of HCNTs, including the controllable synthesis for specific helical morphologies and electronic, magnetic, and mechanical properties.[27−33] Although rapid progress has been made in fabricating crystalline and amorphous carbon micro/nanocoils, the synthesis of HCNTs is still very limited.[31]

Several pioneering experiments have been performed on helical carbons to characterize their mechanical response. Volodin et al.[34] used atomic force microscopy (AFM) to measure a Young modulus of HCNTs of 0.7 TPa. Chen et al.[35] also studied the mechanical properties of an individual carbon nanocoil with AFM and observed a nonlinear springlike behavior with a spring constant 0.12 N/m at low strains and higher spring constants at higher strains. Poggi et al.[36] used AFM to observe the mechanical instability (buckling) of HCNTs. More recently, Yonemura et al.[37] studied the fracture response of carbon nanocoils under uniaxial load and showed that the highest stress concentrations and locations of crack initiation are on the inner edge of the coils. Although these studies have provided valuable information on the observed mechanical response of HCNTs, detailed physical insights into molecular deformation mechanisms have not yet been provided. The fundamental questions concerning the tensile deformation of tightly wound HCNTs can be posed as follows: (1) What is the molecular-structural response of HCNTs loaded in tension? (2) What is the molecular-structural response when unloading? (3) What is the ultimate tensile load that HCNTs can tolerate, and what are the primary failure mechanisms? While the experimental answers to these questions are pending, atomistic modeling can predict the molecular-structural response to tensile loads and provide physical insight into their predicted behavior. The objective of this study is to use atomistic simulations of tightly wound HCNTs to predict their response during tensile loading and subsequent unloading and thus provide physical insight into their mechanical instability, stretchability, nanoscale fracture, and hysteresis loss. This understanding is critical for future use of HCNTs in nanodevices and tough composite materials.

dx.doi.org/10.1021/ja404330q | J. Am. Chem. Soc. 2013, 135, 13775−13785

MODELS AND METHODS

All the calculations were performed using the LAMMPS molecular dynamics simulation package with the adaptive intermolecular reactive empirical bond-order (AIREBO) potential,[38,39] which introduces accurate descriptions of the long-range interatomic interactions (with Lennard-Jones form) into the REBO potential as well as torsional term. The REBO potential is known to accurately model chemical and mechanical properties for hydrocarbons, nanotubes, and diamonds; allowing for the breaking and re-forming of covalent bonds. The cutoff distance for the REBO potential was set to 2 Å (see the Supporting Information) to prevent inaccuracies during the simulated fracture process, as described by Shenderova et al.[40] The long-range Lennard-Jones cutoff distance was set to 10.2 Å. Tightly wound HCNT molecular dynamics (MD) models were constructed consisting of (3,3), (5,3), (7,5), (13,11), (19,17), and (25,23) single-walled carbon nanotube (SWCNT) segments, with the corresponding coil diameter ranging from approximately 1.5 to 16 nm. Pentagon and heptagon carbon ring structures were incorporated into the otherwise pure hexagon structures to accommodate the curvature in the coils of the HCNTs.[15,16,22,30] The MD models consisted of four complete coils along the helical axis, ensuring the length of the helices would be 1-fold larger than the Lennard-Jones cutoff distance. Periodic boundary conditions (PBCs) were applied along the helical axis, which offered unconstrained ends to eliminate any spurious end effects during the deformations, while the perimeters of the simulation boxes were free to simulate stand-alone HCNTs. Prior to the atomistic simulations of uniaxial loading, HCNTs were first quasi-statically relaxed to a local minimum configuration through the conjugate gradient method. Subsequently, the relaxation was performed with a simulation time from 200 to 500 ps, depending on the size of the HCNT and temperature. During the relaxation process, the lengths of as-constructed helixes were allowed to shrink or expand at zero pressure in the PBC direction under an NPT (constant number of particles, constant pressure, and constant temperature) ensemble based on a Nosé−Hoover barostat and Nosé−Hoover thermostat. A time step of 1 fs with the velocity-Verlet integration algorithm was used in all simulations. Parts a and b of Figure 1 show the side and top views of the MD models after relaxation, where the individual atoms are colored according to their cohesive energy. Simulated uniaxial tension under deformation control was performed on the equilibrated HCNT models with a reasonable strain rate of 10^9 s^{-1} [41] by uniformly rescaling the z-coordinate of all atoms in every 100 time steps using an NVT (constant number of particles, constant volume, and constant temperature) ensemble with a Nosé−Hoover thermostat, while allowing the HCNTs to experience a Poisson contraction in the transverse direction of the helical axis. Tensile forces were calculated from the virial stress tensor components on every atom.

RESULTS AND DISCUSSION

As shown in Figure 1a, the least stable covalent bonds (indicated by the red color) are located at the pentagon rings on the outer portions of the coils, while the atoms associated with the heptagons in the inner ridge are the most stable (indicated by the blue color). Furthermore, increases in the size of the HCNT coil diameters lead to increases in the stability of the covalent bonds. It is important to note that these results are in an unloaded state, and internal forces are expected to change as the HCNTs are loaded in tension. From Figure 1b it is evident that the HCNTs have a polygonal shape along the helical axis, and the polygonal shape becomes increasingly distinct as the HCNT diameter increases. From the figure it is also evident that the CNT walls along adjacent coils nearly preserve their original lattice stacking without lattice registry, which has been observed in the collapse of CNTs under pressure.[42] Figure 1c shows the cross-sectional views of the HCNT coils in the equilibrium configuration. The figure indicates that increases in the coil diameter cause a transition of the cross-section from circular to oval-shaped, in agreement with experimental observation (Supporting Information). Furthermore, it is clear that the cross-sections of the larger coil diameters exhibit a flattening of the inner-wall convex portions (in addition to the top and bottom surfaces) and rounded curvature on the outer coil. The cause for this asymmetry in the coil cross-section is the presence of the heptagon-shaped carbon rings on the inside portions of the coils. This is evident by comparing the HCNT coil cross-sections in Figure 1c to the cross-sections of straight CNTs packed in parallel (Figure 1d) and triangular (Figure 1e) lattice arrangements at zero pressure. In the cases of the parallel and triangular lattice arrangements, the CNTs contain only hexagon carbon rings, showing different elastic deformations in the cross-section from HCNTs. Figure 1d displays the progression of the geometrical shape from circular rigid cylinders to a racetrack-like shape for increasing coil diameters. A racetrack shape is maintained instead of a peanut shape because of the higher binding energy between adjacent adhering intertube walls than that of intratube walls. Zang et al.[43] discovered that the ratio of the area of the tubular cross-sections at the transition from oval or racetrack to peanut appears as a constant of about 0.819469. Interestingly, the semicircular caps in the racetracks demonstrate a constant diameter of roughly 1.5 nm as plotted in Figure 2, indicating the existence of a

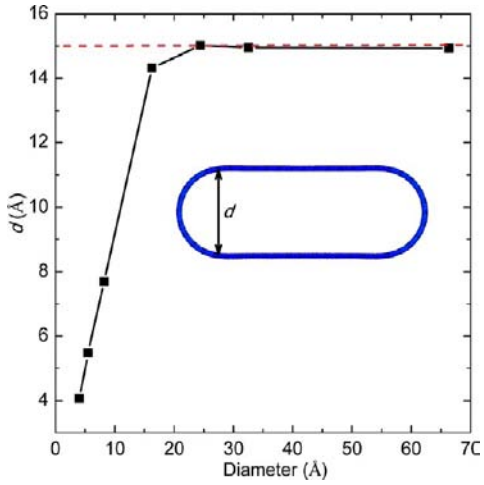

Figure 2. Degree of flattening of CNTs when they are packed in a parallel arrangement. As illustrated by the inset, a racetrack-like shape is found in the large-diameter CNT, where the diameter of semicircular caps, d, is constant when the original diameter of the CNT is larger than 24 Å.

geometric constant that defines large SWCNT shape transition in the case of parallel arrangement (Figure 1d). From Figure 1e, there is a transition from circular to rounded-hexagon CNTs with increasing diameters, and the polygonization of CNTs starts with CNT diameters of about 1.6 nm, which are consistent with previous simulations and experiments.[44,45] The changes in coil shapes shown in Figure 1c−e with increasing diameters originate from a balance between the curvature elasticity and the intertube van der Waals (vdW) interaction. The perfect hexagonal ring structure in the parallel and triangular lattice structures leads to the symmetric deformed cross-sections, while the presence of heptagon rings on the inner surface of the HCNT coil results in asymmetry between the inside and outside surfaces. The heptagonal defects cause a

dx.doi.org/10.1021/ja404330q | J. Am. Chem. Soc. 2013, 135, 13775−13785

localized increase in bending rigidity, which makes the radial elastic deformation energetically unfavorable, and thus the flattened surface on the inner side of the coils.

To further emphasize this point, Figure 3 compares the calculated energy per atom versus the radii of the CNTs in the three arrangements, where the energy per atom in the HCNTs is obtained by excluding the pentagon defects which introduce highly localized excessive energy. As expected, for all three CNT bundle forms, the energy per atom decreases with increasing diameters and, eventually, approaches the value of graphite. The magnitudes of energy per atom for the same diameter CNTs, however, show the order helix > parallel > triangular lattice arrangement. This suggests that a CNT bundle with a two-dimensional triangular lattice possesses a lowest energy configuration and is more frequently observed. Furthermore, it can be seen that remarkable high energy per atom for the smallest helix mainly comes from dense embedment of heptagon defects.

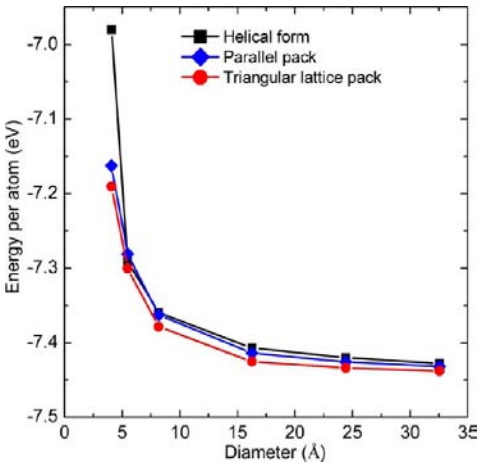

Figure 3. Average energy per atom versus diameter of CNTs packed in parallel, triangular lattice, and tightly wound helical forms. The pentagon defects in the HCNTs are excluded.

A set of tension tests were performed to rupture at a low temperature (1 K) to evaluate the overall deformation behavior of HCNTs. Parts a–f of Figure 4 show the resulting global stretching force–elongation curves for the (3,3), (5,3), (7,5), (13,11), (19,17), and (25,23) HCNTs, respectively. The extension can be roughly divided into three stages.

In the first stage, a steep increase of stretching force occurs. From each initial linear stretch-extension curve, the stiffness of the HCNTs with four turns was calculated to be 19.48, 12.57, 30.71, 21.92, 17.30, and 13.79 nN/nm, respectively, for the increasing HCNT sizes. These stiffnesses are about 2 orders of magnitude greater than those measured in experiments (sparsely coiled HCNTs), mainly due to strong vdW interaction between adjacent HCNT walls and a smaller size comparable to that of experimental specimens.[32,33,35] For clarity, the initial stretch-elongation curves of Figure 4 are shown in Figure 5. Prior to the first peak, nonlinearity is observed in small HCNTs, while linearity occurs in large HCNTs. The magnitude of the critical extension force for the former case is about 3 times larger than that of the latter case, while the Young modulus is 1 order of magnitude smaller than that of the large case due to the large cross-sectional area.

In the second stage of deformation, a significant straightening of HCNTs occurs, which leads to the characteristic sawtooth pattern in the tension force–elongation curves in Figure 4. For

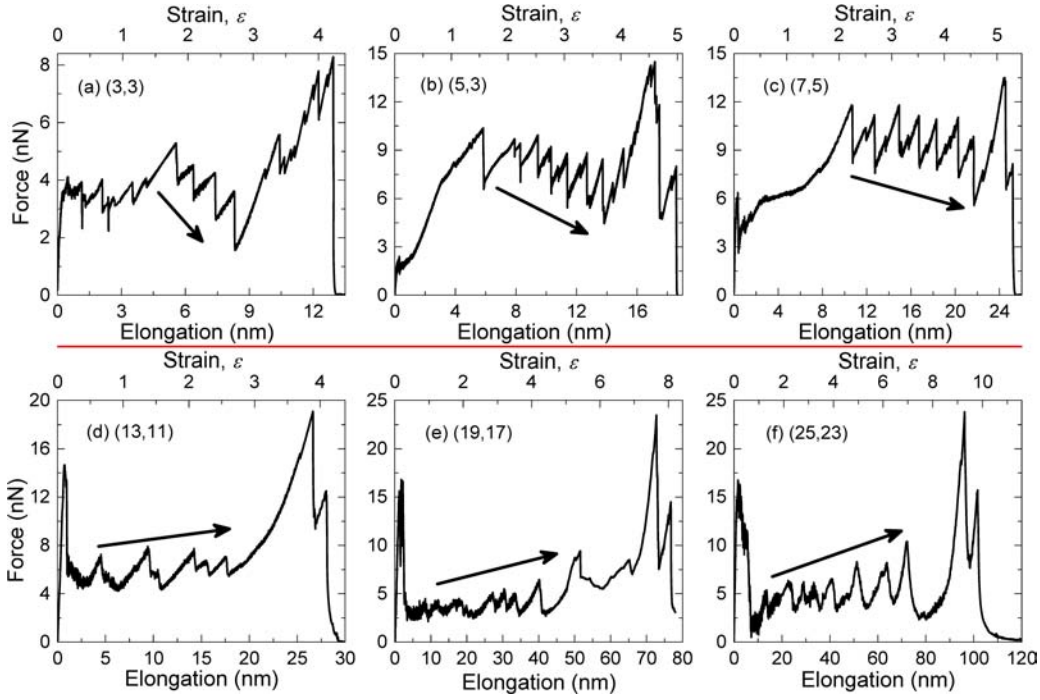

Figure 4. Tensile force versus elongation (strain) curves of tightly wound HCNTs, with a sawtooth pattern resembling those of a stepwise unfolding of biomolecule domains. The helical morphology of CNTs allows stretching to very large strains varying from 400% to 1000%, suggesting remarkable energy required to rupture. As marked by the arrows, the peaks of stepwise loads display two different trends, depending on the HCNT size. The HCNTs resist pulling to a high force in the range of 10–20 nN before complete rupture. The last two peaks of each HCNT correspond to their final rupture, where the appearance of a small peak at the end results from the stretching of a single monatomic carbon chain.

dx.doi.org/10.1021/ja404330q | J. Am. Chem. Soc. 2013, 135, 13775–13785

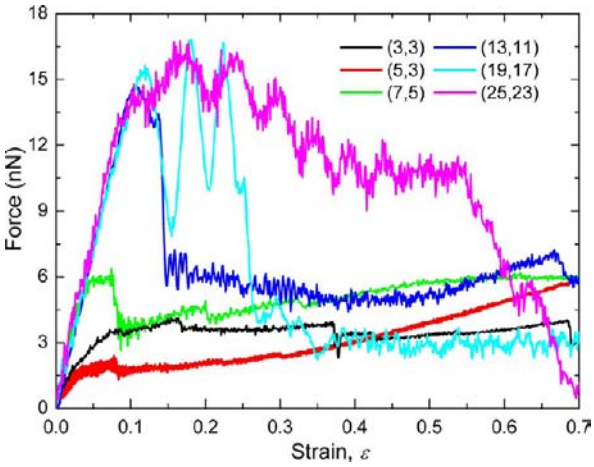

Figure 5. Tensile loading curves of the HCNTs in the low-strain regime. An initially steep slope is due to the strong vdW interactions between intertube walls. The larger force at the first peak of the (3,3) HCNT compared to that of (5,3) HCNT mainly comes from higher vdW attractive forces between the four adjacent coils.

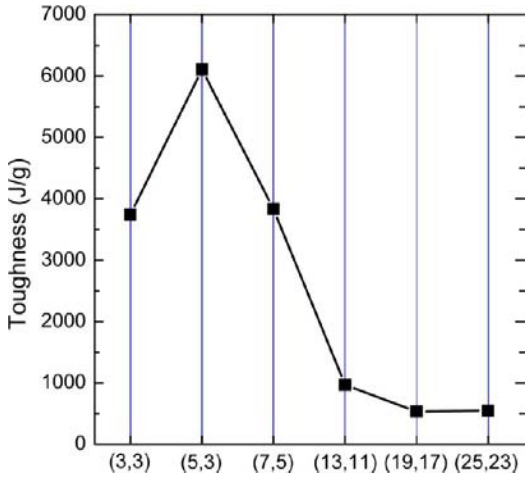

Figure 6. Gravimetric toughness of the HCNTs evaluated from the tensile curves, varying from 500 to 6200 J/g, which is size dependent. The high density of defects in the (3,3) HCNT mainly leads to the smaller toughness relative to that of the (5,3) HCNT.

the three small HCNTs, a dramatic growth in load after the first drop immediately turns up compared with that of the three large cases, followed by a steeper load drop than that of the large cases. The number of sawtooth steps observed in the curves is greater than that of coils, indicating the occurrence of multiple structural transformations of HCNTs during elongation. Interestingly, a decrease of peak loads appears with increasing elongation for the three small HCNTs (marked by the arrows in Figure 4), while the three large cases exhibit the opposite trend, representing two distinct deformation modes. Indeed, these two opposite behaviors reflect a successive break-vs-arrest process in the small HCNTs and opening and straightening of loops within large HCNTs, respectively (see the next section). The spanned distance between adjacent peaks depends on the coil diameter and is more uniform in the three small HCNTs, and the numbers of peaks would depend on the number of helical turns. The curves of the sawtooth pattern for the three large cases can be described well by the wormlike chain (WLC) model.

The third stage is associated with a rapid increase in load, followed by a complete drop of the load. Overall, the whole tensile force−elongation curves show strong nonlinearity, indicating complex deformation of HCNTs due to a combination of bending, torsion, and tension stresses in the HCNTs. All six deformation curves demonstrate that the HCNTs are capable of sustaining axial strains in the range of 400−1000%, comparable to the mechanics of unfolding a stacked biomolecule. The gravimetric toughness (total energy absorbed per unit mass) is evaluated from the force−elongation curves using

$$E_T = \frac{E_{rupture}}{m} = \frac{\int Fx\, dx}{\frac{Nm_C}{NA}} \quad (1)$$

where $E_{rupture}$ is the applied energy to rupture, m is the mass of HCNTs, F is the applied axial force, x is the axial elongation, N is the number of carbon atoms in the HCNTs, m_C is the mass of carbon atoms, and NA is Avogadro's constant. The gravimetric toughness values for each of the HCNTs are plotted in Figure 6. The toughness values vary from 540 to 6200 J/g, with the maximum occurring for the (5,3) system, which is slightly higher than but of the same magnitude as that of a perfectly straight CNT,[46] and the minimum for the largest two HCNTs. There is a clear size effect trend of decreasing toughness values for increasing HCNT sizes, except for the smallest system. The relatively low toughness of the (3,3) HCNT is most likely caused by its high density of structural defects for the formation of its small spring structure. Similarly, springlike CNT ropes have been fabricated by a conventional spinning technique to withstand large axial strains, reaching a toughness of only 28.7 J/g.[47] The relatively large toughness of the HCNTs makes them an ideal reinforcement for lightweight structural composites.

To gain physical insight into the deformation mechanisms of HCNTs, it is instructive to examine the specific atomic configurational evolution of the three deformation stages discussed above. The instant structural developments of two representative HCNTs under tension were monitored. Figure 7 shows a series of snapshots of the (5,3) HCNT during axial deformation in tension. Before stretching, the coils are regular, where the intertube spacing d, as illustrated by the parallel dash lines in Figure 7a, has a magnitude of 3.35 Å. Because of their complex geometry, it is expected that HCNTs will experience a combination of tension, bending, and torsion stresses whose proportions depend on the pitch angle and tube and coil diameters. Initially, the stretching of the HCNT is dominated by the increase of the intertube spacing via the vdW interaction between intertube walls, which induces the initial stiffness shown for the (5,3) HCNT in Figure 5. Once the HCNT is pulled to a sufficient length, diminishing the vdW interactions between intertube walls and releasing excess strain energy (Figure 7b), the first significant drop of tensile force for the (5,3) HCNT is observed (Figure 5). As the applied strain continues to increase, more instances of uncoiling occur (Figures 7c−e), each corresponding to observable sudden drops in the stress−strain response. The result is the first stage of the stress−strain response discussed above.

As the strain continues to increase beyond the first stage and into the second stage, an increase of stress on the inner edge of the HCNT coils is clearly observed (Figure 7f), which is in excellent agreement with experimental observation.[37] From the top view motifs in Figure 7, it can be observed that, for strains

dx.doi.org/10.1021/ja404330q | J. Am. Chem. Soc. 2013, 135, 13775−13785

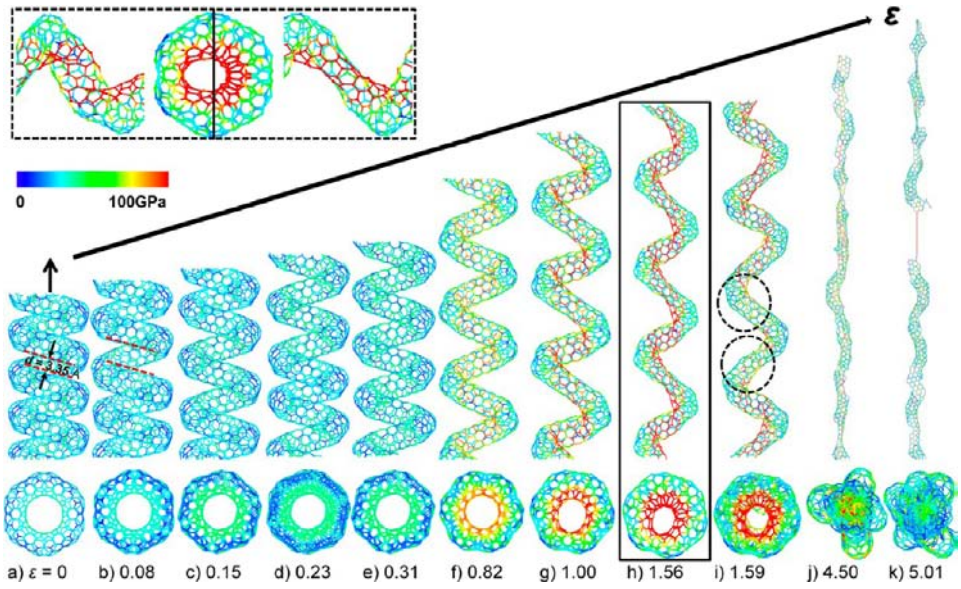

Figure 7. Atomic structural evolution of the (5,3) HCNT during tension loading. In the equilibrium state, the intertube distance has a typical value of 3.35 Å, with no sign of stress concentration located at the introduced defects. The initial stretching to strain of 31% clearly leads to the stepwise detachment of intertubes without dramatically increasing stress at the inside of the helix. From 31% to 82% strain, homogeneous deformation induces significant stress concentration situated at the inside. After 82% strain, mechanical instability gradually emerges in terms of two distinct bucking patterns, stretch and torsion domination, as seen in the inset with high stress concentrations on the inner surface. A series of break−arrest events leads to HCNT straightening, reaching 500% strain to complete rupture. In addition, the top view motifs of the HCNTs visibly display a ∼40° twist of the HCNTs upon mechanical instability, followed by very small further twisting to fracture. Atoms are colored on the basis of von Mises stress.

up to around 82%, a significant amount of twisting of the HCNT occurs. However, as the strains increase beyond 82%, the top view motifs demonstrate axial asymmetry, which is indicative of the formation of buckles. The inset in Figure 7 shows two buckle modes: twisting (left) and collapse (right). The presence of these two buckle patterns leads to the asymmetric appearance that begins at a strain of 100% (Figure 7g). From Figure 4b, there is a significant load drop between 156% and 159% strain, which is the beginning of the characteristic stage 2 sawtooth patterns. Examination of parts h and i of Figure 7, which correspond to the states immediately before and after this load drop, respectively, reveals that the release in the load is due to local fracture initiated at defects, indicated by the dashed ovals in Figure 7i. The local fracture is immediately arrested because of the loss in concentrated stresses near the fracture points. Further increases in strain are accompanied by a succession of such localized fractures, which is responsible for the sawtooth appearance in the tensile force−elongation curve (Figure 4b).

In the third stage of loading, the highly elongated and fractured HCNTs become straight and taut (Figure 7j), causing the significant increase in tensile force shown in Figure 4b at a strain of 450%. Continued fracture events of the carbon ring structures eventually lead to the stretch of a single monatomic chain (Figure 7k), which is the source of the last peak in the curve of Figure 4b close to a strain of 500%. Due to the large amount of damage to the structure of the HCNT at this level, the broken segments do not recoil when unloaded. Figure 8 shows the deformation characteristics of the (25,23) HCNT. Comparison between Figures 7 and 8 reveals a significant difference in the deformation behavior between the small and large HCNTs, despite the similarities between the three phases of force−elongation behaviors (Figure 4b,f). From Figure 8, it is evident that there are higher intrinsic stresses at the pentagon defects of the HCNT throughout the deformation process, similar to higher potential energy data shown in Figure 1a. During the first stage of the deformation process, the intertube spacing is preserved while the coil cross-section is distorted, as shown in Figure 8a,b, corresponding to the initial steep load in the force−elongation curve shown in Figure 5. Increases in the axial strain are accommodated by the sliding of the coils with respect to each other, as shown in Figure 8c,d. Because of the large surface area of the coils in this large HCNT, the binding energy between adjacent coils is too strong to overcome in this stage by direct separation. However, a sliding action between the coils requires much less energy. The coils reorient themselves in a direction 45° from the global deformation axis to allow sliding to occur on the planes with the maximum shear stress, as clearly shown in Figure 8d. In Figure 4, it is clear that the effect of this sliding is a flattened force−strain response up to an axial strain of 55%. When the coils have oriented themselves along the planes of maximum shear stress, further axial deformation must be accommodated by another mechanism. In Figure 8c, localized kinking is observed between pentagonal defects. The onset of kinking gives rise to a redistribution of local strains in the HCNT, as can be seen in Figure 8e with the nonuniform shape of the HCNT. The nonuniform shape also exhibits reductions in local contact area between some adjoining coils. The development of kinks causes a substantial release of the axial load at strains around 60%, as shown in Figure 4. Eventually, the presence of local kinks and the reduction in the contact area between coils leads to the complete collapse and separation of adjacent coils in the vicinity of the kinks, as seen in Figure 8f. These events lead to a large relaxation of the HCNT structure (Figure 8f) and the lowest loading point in Figure 4f. Figure 8f clearly shows the buckled HCNT coils and the first separation of the coils in the area where the kinks originally formed, as shown in Figure 8e.

dx.doi.org/10.1021/ja404330q | J. Am. Chem. Soc. 2013, 135, 13775−13785

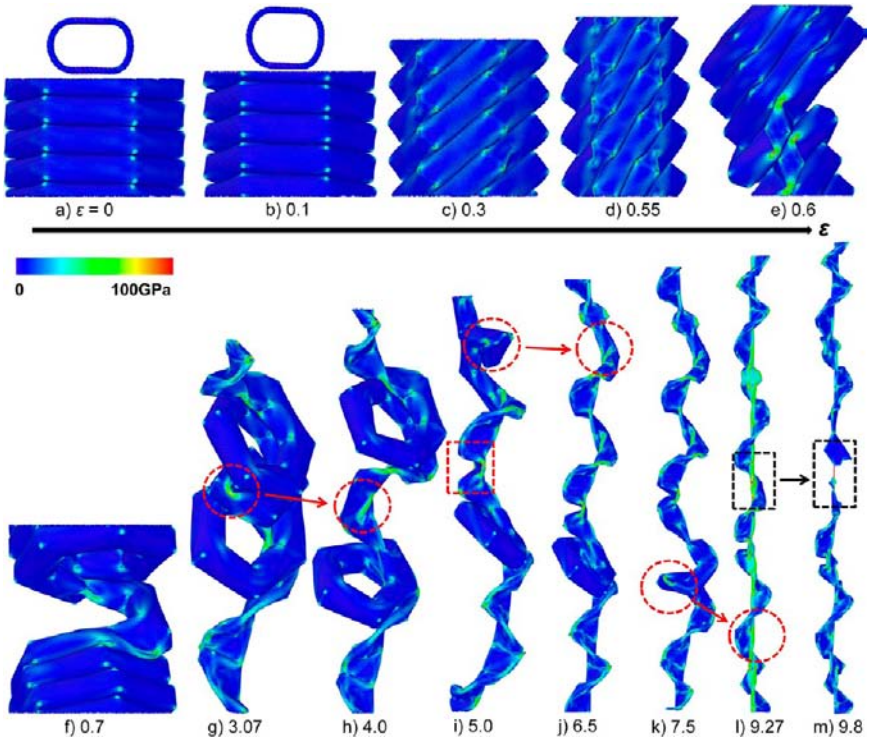

Figure 8. Atomic structural development of the (25,23) HCNT during tension loading. Before loading, a moderate amount of coil flattening exists, which is partially removed during the first stage of loading. Reorientation of the coils follows without any immediate coil separation, differing with the small case. With further increases in strain, the appearance of wrinkles facilitates a further reorientation of coils. At a strain of around 60%, the collapse of a single coil is observed. Both reorientation of coiling and the collapsed CNT segments tightly adhering to neighboring intertubes result in decoiling of the middle coil, forming two mutually perpendicular finlike, locally flattened areas. With further extension, the residual coils are opened one after another. During the decoiling process, the coils yield at the heptagon defects to form tight knots. The knots are able to tactfully untie without loss of buckling. Finally, all the coils are straightened to form a helical edge-closed graphene ribbon. Further straightening leads to significant stress concentrations on the inner edge of the helical ribbon. A single fracture initiated at a heptagonal defect to complete rupture can be observed at a giant rupture strain of ∼1000%. The atoms are colored according to von Mises stress.

The second stage of loading for the (25,23) HCNT is characterized by a series of these kinking−buckling−separation mechanisms and gives rise to the characteristic sawtooth pattern observed in Figure 4f between strains of about 1% and 8%. After the first coil separation shown in Figure 8f, further increases in axial strain are accommodated by the straightening of the uncoiled portion of the HCNT. The tension developed in the uncoiled portion causes kinks to appear between the pentagonal defects in the coils (red circle in Figure 8g), which are released when the coil finally collapses and uncoils (red circle in Figure 8h). A kink remains in this location after the coil is released (red box in Figure 8i). Upon further axial elongation, the residual coils are released in a similar manner (Figure 8i−l), leading to the sawtooth pattern. From Figure 4f, it can be seen that the critical force required to unfold the coils increases with increasing strain.

The final stage of the loading of the (25,23) HCNT begins when all of the coils have been released (Figure 8l). After the unfolding of all the coils, what essentially remains is a graphene ribbon helix with local rigid pentagon defects. As intuitively expected, the developed stresses are mainly focused on the inward edge of the helix. Continued straining of the helical ribbon finally results in fracture initiated at a heptagon defect with a high stress concentration, as shown in the black box in Figure 8l. Prior to complete separation, a monatomic chain forms (Figure 8m), which is typically observed in CNTs before complete failure. Following complete rupture, the broken segments recoil quickly toward their respective ends, similar to the experimental observation for Si_3N_4 microcoils.[48]

Previous studies have shown that the large tensile ductility of straight CNTs originates from defect nucleation and motion.[9−12] It has also been found that temperature governs the buckling behavior of SWCNTs,[49,50] and the buckling configuration can be either global or local.[51] Additionally, the presence of defects in the hexagonal network commonly degrades the extraordinary mechanical properties of CNTs, and the degree of degradation is strongly dependent on the temperature.[50] Because CNT mechanical behavior is strongly affected by the temperature, it is important to explore the role of temperature in the mechanical response of HCNTs with pre-existing periodic defects. Parts a and b of Figure 9 present the simulated force−strain response for the (5,3) and (13,11) HCNTs, respectively, at temperatures varying from 1 to 1000 K. Overall, the curves show substantial tensile ductility over the complete temperature range for both HCNTs. Prior to initial yielding, as marked by the gray-shaded region in Figure 9, the overlapping curves indicate that the mechanical response of both HCNTs is insensitive to the temperature. From Figure 9a it is evident that the (5,3) HCNT exhibits a characteristic sawtooth pattern, suggesting that the deformation mechanisms discussed above are not altered by the temperature change. However, the elastic limit, the critical strain at complete rupture, and the magnitude of the stepwise loads decrease significantly at higher temperatures. For the (13,11) HCNT, it is readily seen from Figure 9b that temperature does not play a

dx.doi.org/10.1021/ja404330q | J. Am. Chem. Soc. 2013, 135, 13775−13785

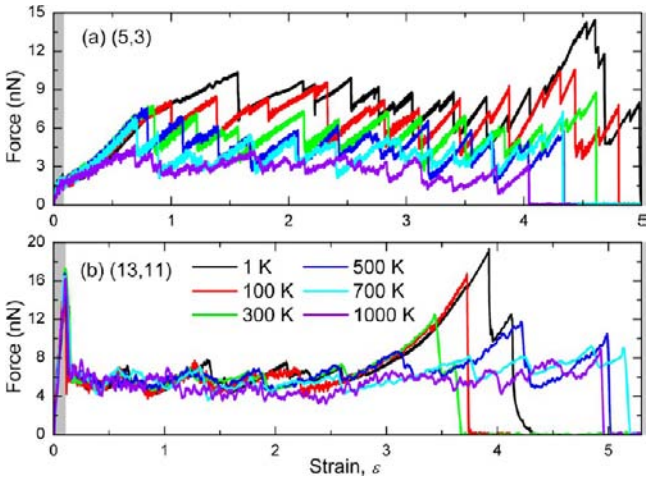

Figure 9. Tensile force−strain curves of two (5,3) and (13,11) HCNTs at various temperatures from 1 to 1000 K. As seen in the gray-shaded area, the initial mechanical response mainly coming from the vdW interaction between intertube walls is insensitive to the temperature. Beyond this initial stretching, the temperature plays a key role in the mechanical response of the smaller HCNT. Increases in temperature result in reductions in the tensile ductility. For the large HCNT, a reduction of tensile ductility is found at lower temperatures, while an enhancement of tensile ductility is found at higher temperatures.

significant role in the mechanical response for axial strains below 250%. After 250% strain, the force gradually rises with further elongation at lower temperatures, reaching a critical load that increases with decreasing temperatures. The temperature-dependent critical loads are followed by deep load drops, indicating the complete failure of the HCNT.

Figure 10a shows snapshots of the (5,3) HCNT just before initiation of fracture for a wide range of temperatures. These results indicate that increases in temperature lead to decreases in the initiation to failure. At higher temperatures, the atoms have larger vibration amplitudes, which lead to a greater chance of fracture initiation occurring at lower strains. The higher elongation at lower temperatures allows for more occurrences of coil buckling as can be observed in Figure 10a. Figure 10b shows snapshots of the (13,11) HCNT prior to complete failure at various temperatures. There does not appear to be a distinct relationship between temperature and strain to failure (consistent with Figure 9b), and complete buckling of the coils occurs prior to failure in each of these cases. It is interesting to note that, in the case of the (13,11) HCNT at 1000 K, further elongation is limited by the inability of two knots to untangle. Comparison of Figures 7−10 indicates that the smaller and larger HCNTs have comparable toughnesses at lower temperatures, and larger HCNTs tend to have a higher toughness at elevated temperatures. The higher defect density of the smaller HCNTs leads to a greater resistance to buckling during elongation. The ability of the larger HCNT coils to completely buckle and straighten makes them tougher than the smaller HCNTs at the higher temperatures.

To evaluate the mechanical energy damping capability of HCNTs, cyclic loading simulations were performed on the (5,3) HCNT. The simulated temperature was 1 K to eliminate thermal effects. A strain amplitude of 150% was applied since the first failure event occurs in this HCNT at 1 K at a strain of 159% (Figure 9a). Figure 11a shows the force−elongation curves of the (5,3) HCNT for a single loading−unloading cycle. In accordance with the above discussion about the individual deformation mechanisms associated with this HCNT, region A of Figure 11a corresponds to the initial loading, region B corresponds to the twisting of the HCNT and the reduction in vdW bonding between adjacent coils, and region C corresponds to the small buckling events that occur before fracture initiation (see Figure 7). The unloading path traces the loading path almost completely, with the red-shaded areas indicating regions of hysteresis. Therefore, in this domain of elongation, the long-range vdW interactions that initially exist between coils are re-established during unloading, and the

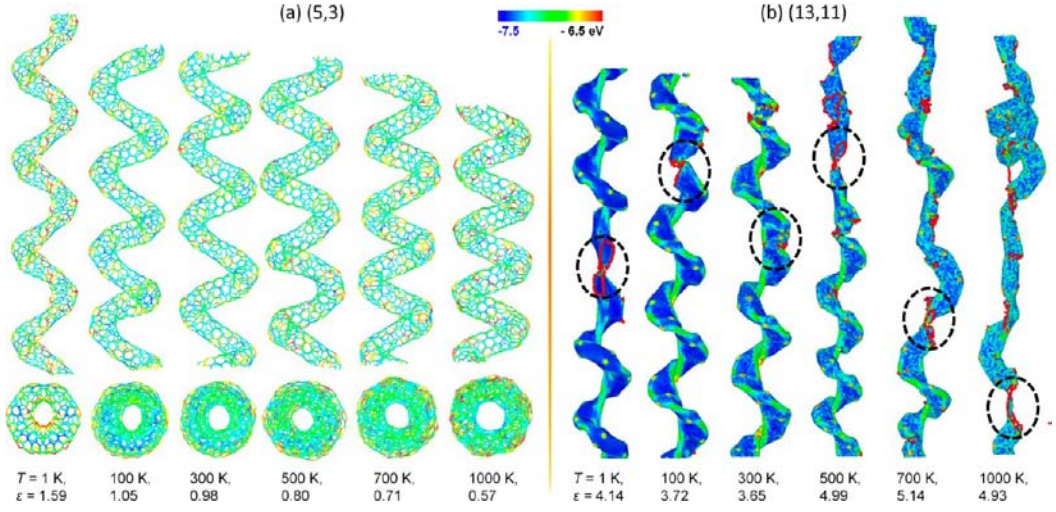

Figure 10. Snapshot configurations of deformed HCNTs at various temperatures from 1 to 1000 K. (a) Side and top views of the (5,3) HCNT just before initial fracture. Clearly, the buckling behavior is not observed at high temperature, which provides high-energy agitation to overcome the energy barrier for fracture. (b) Side view of the (13,11) HCNT prior to complete rupture. The number of local fractures in the HCNT depends on the temperature. The successive local fractures are well-distributed and thus enhance the ductility. Two distinct buckling modes corresponding to stretch and torsion domination occur in the HCNT stretching. Interestingly, there are two residual coils in the highly strained HCNT before complete rupture. Atoms are colored according to the potential energy. The dashed oval represents the location of the fracture that causes complete rupture.

dx.doi.org/10.1021/ja404330q | J. Am. Chem. Soc. 2013, 135, 13775−13785

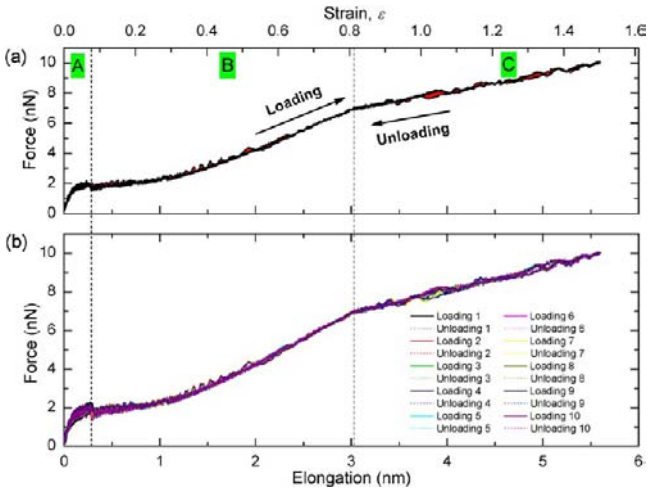

Figure 11. Loading–unloading tensile curves of the (5,3) HCNT for 10 cycles with a preset strain of 150%. The red-highlighted area in the top figure depicts the hysteresis. The dashed lines represent two distinct structural transformations: detachment of two adjacent intertubes and buckling. The buckling mode corresponding to "gradual" buckle formation results in the unloading of the stretched HCNT almost retracing the loading curves, reflecting no energy dissipation.

twisting and buckling that occur are completely reversible. The negative incremental stiffness of HCNTs is not the same as experimentally observed and quantified in terms of buckling mechanics for axially compressed MWCNTs by Yap et al.[52] Figure 11b shows 10 loading–unloading cycles and signifies that the reversibility observed in Figure 11a is highly reproducible.

Figure 12 shows the cyclic loading response of the (13,11) HCNT. Typical morphological changes that occur during a single loading and unloading cycle are shown in parts a and b, respectively, of Figure 12. The force–elongation responses are shown in Figure 12c. Similar to the response of the (25,23) HCNT shown in Figure 8, the loading behavior of the (13,11) HCNT shown in Figure 12a indicates that the coils separate individually when subjected to axial strain with nearly simultaneous buckling of the coil cross-section in the region of the coil separation. This decoiling–buckling process is characterized by the first major loss in load around a strain of 15%. The energy required to cause the elastic deformation, local buckling, and coil separation is the area under the force–elongation curve in Figure 12c. Further elongation results in more coil separations at strains of about 65%, 140%, and 190%, resulting in the sawtooth-like force–elongation curve. Under a tensile strain of 210%, the (13,11) HCNT coils are completely separated and buckled to resemble a helical edge-closed graphene ribbon. Upon unloading from a strain of 210%, the force curve follows a different path. The unloading behavior does not have the characteristic sawtooth pattern of the loading behavior. The differences between the loading sawtooth pattern and the smoother unloading pattern are highlighted in red in the inset in Figure 12c. Clearly, the larger discrepancies occur for strain levels corresponding to uncoiling–buckling events during the loading portion of the cycle. Therefore, the amount of mechanical energy required to separate and buckle the coils is not completely returned when the HCNT is unloaded, even though the HCNT configuration in the completely unloaded state (strain 0%) looks identical to the configuration before

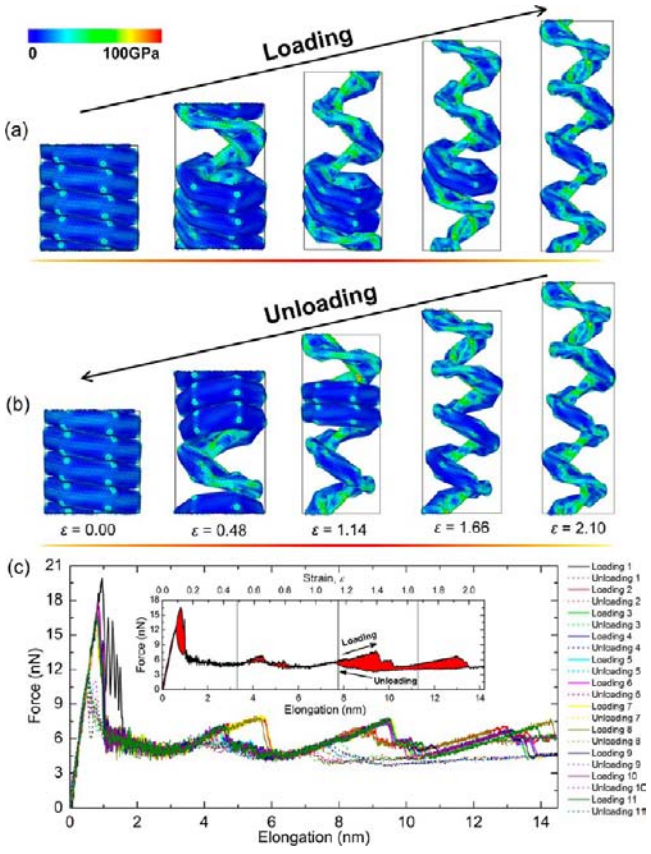

Figure 12. Cyclic loading for giant stretchable tightly wound (13,11) HCNTs. (a, b) Snapshots of 10 representative configurations of the (13,11) HCNT for the fifth cyclic loading. The images clearly demonstrate that two distinct structural configurations are observed in the intermediate loading cycle, indicating two strikingly different paths. (c) Cyclic loading–unloading tensile curves of the (13,11) HCNT for 11 cycles with a preset strain of 210%, showing two distinct loading–unloading paths. The strain dropped by lines in the inset corresponds to the above three intermediate configurations during cyclic loading. The red-highlighted area in the inset mainly composed of several closed loops which closely relate to buckling of the coils, depicting the hysteresis, represents the energy dissipated during a loading–unloading cycle. Atoms are colored according to von Mises stress.

loading occurred. From Figure 12c, remarkable reproducibility of this behavior is confirmed.

The cause of the hysteresis with the (13,11) HCNT can be explained with a closer examination of the force–elongation behavior at relatively small strains. Figure 13 shows the mechanical response of the (13,11) HCNT for 10 cycles of loading–unloading at a strain of around 30%. During the first loading cycle, the HCNT has a linear response up to a strain of nearly 15%, where the load drops to around 12 nN. Immediately following this load drop is a brief rise in the load followed by another load drop to around 6 nN, where it remains nearly constant up to a strain of 30%. The time period between the load drops is very small, indicating that the two events occur almost simultaneously. Upon unloading, the mechanical response is different. At a strain of about 10%, the unloading curve has its first significant rise in the load. The slope of the unloading curve at this point has the same slope that the loading curve has during its first significant load drop, as indicated by the blue rhomboid. Because the slopes are the same, it is clear that the load drop–rise in these regions is due

dx.doi.org/10.1021/ja404330q | J. Am. Chem. Soc. 2013, 135, 13775–13785

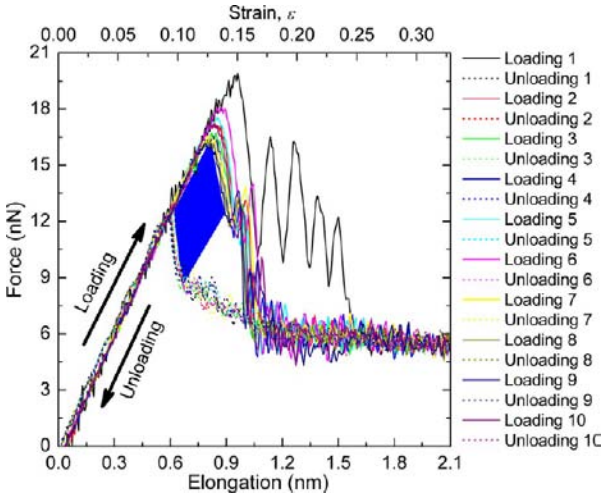

Figure 13. Cyclic loading–unloading tensile curves of the (13,11) HCNT for 10 cycles with a predefined low strain. The stable dissipation energy enclosed by the inset blue rhomboid, decomposed from the hysteresis loop, results from the stable vdW force between adjacent intertube walls. Another area decomposed from the hysteresis loop represents the mechanical instability corresponding to the buckling of one coil confirmed by the following peaks under loading and unloading.

to the same mechanism. It is also clear that the total mechanical energy that is input into the system is not fully recovered when unloaded.

The likely explanation for this behavior is as follows. The first significant load drop during the loading cycle is associated with the breaking of vdW bonds between adjacent coils in the HCNT. This uncoiling action is immediately followed by the complete buckling of the coil in the region of the uncoiling. These two events occur almost simultaneously, resulting in a total load drop of 12 nN. During the loading process, the total mechanical energy put into the system (area under the curve of Figure 13) is used for elastic deformation, breaking of vdW bonds, and buckling of the coils, each of which require mechanical work. During unloading, the mechanism that causes the load rise must be the formation of vdW bonds between the coils, since the slope matches that associated with breaking vdW bonds in the loading cycle. This rise in loads brings the unloading curve to its highest peak, which is about 6 nN smaller than the loading peak, after which the force decreases in a linear-elastic manner. Therefore, the mechanical energy restored in the system during the unloading process is due to elastic and vdW effects alone, without the influence of the unbuckling of the coils. Thus, the energy required to unbuckle the coils is not mechanical energy, but thermal energy supplied by the system.

During the MD simulation of the loading, the NVT ensemble was used, and the energy released by the breaking of vdW bonds is partially used to overcome a local energy barrier and collapse the HCNT coils. The remainder of the energy, along with the additional energy associated with the buckling, is eventually absorbed by the environment to maintain a constant temperature. This is achieved by the Nosé–Hoover thermostat. During the unloading, there is not enough energy available to overcome a local energy barrier to unbuckle the coils. Instead, the buckled coils are brought close enough together to re-form the previously broken vdW bonds. The energy required to do this comes from the environment (again, via a thermostat). Once the vdW bonds are established, the walls of the coils seek an equilibrium spacing between each other, which leads to the natural unbuckling of the coils at no additional energy cost. Therefore, the mechanical energy put into the system is partially converted to thermal energy, which leads to an excellent mechanical energy dissipation mechanism. This analysis was repeated in the NVE ensemble for verification (Supporting Information).

CONCLUSIONS

This study focuses on the atomistic simulation of stretching instability and hysteresis of tightly wound HCNTs under uniaxial tension and cyclic loading. In equilibrium, flattening of tightly wound HCNTs occurs due to vdW interactions between intertube walls. This flattening is prohibited by embedded defects. Stretching of the HCNTs can be divided into several stages. The initial steep increase in the force–elongation curve originates from vdW interactions between intertube walls. In the second stage, a characteristic sawtooth pattern emerges in the mechanical response. For small HCNTs, this behavior originates from distributed partial fractures that occur along the length of the coils. For the large HCNTs, the sawtooth pattern is caused by a combination of localized slipping, buckling, and separation of coils. The final stage is associated with a dramatic rise in the load followed by complete rupture of the HCNTs. Under cyclic loading, large HCNTs show pronounced hysteresis loops resulting from the recoverable buckling and vdW bonding between intercoil walls. Furthermore, the unloading curves demonstrate an unprecedented negative stiffness behavior in which increasing tensile forces are required to completely unload the material. The combination of these deformation mechanisms behind the giant stretchability and ideal reversibility of HCNTs sheds new light on the design and application of materials with outstanding performance.

ASSOCIATED CONTENT

Supporting Information

Description of the atomic model of tightly wound HCNTs compared with experimental observation, cutoff distance for the breaking of the C–C bond in the AIREBO potential, comparison of the tensile test of the (5,3) HCNT under two different loading techniques, comparison of the cyclic loading test of the (13,11) HCNT under two different thermodynamic ensembles, atomic coordinates of HCNTs, Figures S1–S10, and videos S1–S6 showing molecular simulation of the mechanical property tests. This material is available free of charge via the Internet at http://pubs.acs.org.

AUTHOR INFORMATION

Corresponding Author

zhiliang.zhang@ntnu.no

Notes

The authors declare no competing financial interest.

ACKNOWLEDGMENTS

This work is supported by the Research Council of Norway (RCN) under NANOMAT KMB (MS2MP) Project No. 187269, and the computational resources are provided by The Norwegian Metacenter for Computational Science (NOTUR).

REFERENCES

(1) Iijima, S. *Nature* **1991**, *354*, 56–58.

(2) Saito, R.; Dresselhaus, G.; Dresselhaus, M. S. *Physical Properties of Carbon Nanotubes*; Imperial College Press: London, 1998.
(3) Dresselhaus, M. S.; Dresselhaus, G.; Eklundm, P. C. *Science of Fullerenes and Carbon Nanotubes: Their Properties and Applications*; Academic Press: San Diego, CA, 1996.
(4) Peng, B.; Locascio, M.; Zapol, P.; Li, S.; Mielke, S.; Schatz, G.; Espinosa, H. D. *Nat. Nanotechnol.* **2008**, *3*, 626−631.
(5) Treacy, M. M. J.; Ebbesen, T. W.; Gibson, J. M. *Nature* **1996**, *38*, 678−680.
(6) Wong, E. W.; Sheehan, P. E.; Lieber, C. M. *Science* **1997**, *277*, 1971−1975.
(7) Yakobson, B. I.; Campbell, M. P.; Brabec, C. J.; Bernholc, J. *Comput. Mater. Sci.* **1997**, *8*, 341.
(8) Belytschko, T.; Xiao, S. P.; Schatz, G. C.; Ruoff, R. S. *Phys. Rev. B* **2002**, *65* (23), 235430−235437.
(9) Ding, F.; Jiao, K.; Wu, M.; Yakobson, B. I. *Phys. Rev. Lett.* **2007**, *98*, 075503.
(10) Huang, J. Y.; Chen, S.; Wang, Z. Q.; Kempa, K.; Wang, Y. M.; Jo, S. H.; Chen, G.; Dresselhaus, M. S.; Ren, Z. F. *Nature* **2006**, *439*, 281.
(11) Huang, J. Y.; Chen, S.; Ren, Z. F.; Wang, Z. Q.; Wang, D. Z.; Vaziri, M.; Suo, Z.; Chen, G.; Dresselhaus, M. S. *Phys. Rev. Lett.* **2006**, *97*, 075501−075503.
(12) Tang, C.; Guo, W.; Chen, C. *Phys. Rev. B* **2009**, *79*, 155436−155444.
(13) Yakobson, B. I.; Brabec, C. J.; Bernholc, J. *Phys. Rev. Lett.* **1996**, *76*, 2511−2514.
(14) Kutana, A.; Giapis, K. *Phys. Rev. Lett.* **2006**, *97*, 245501−245504.
(15) Dunlap, B. I. *Phys. Rev. B* **1992**, *46*, 1933−1936.
(16) Itoh, S.; Ihara, S.; Kitakami, J. *Phys. Rev. B* **1993**, *48*, 5643−5647.
(17) Zhang, X. B.; Zhang, X. F.; Bernaerts, D.; van Tendeloo, G.; Amelinckx, S.; van Landuyt, J.; Ivanov, V.; Nagy, J. B.; Lambin, Ph.; Lucas, A. A. *Europhys. Lett.* **1994**, *27*, 141−146.
(18) Amelinckx, S.; Zhang, X. B.; Bernaerts, D.; Zhang, X. F.; Ivanov, V.; Nagy, J. B. *Science* **1994**, *265*, 635−639.
(19) Cui, R.; Han, Z.; Zhu, J. J. *Chem.—Eur. J.* **2011**, *17*, 9377.
(20) Lau, K. T.; Lu, M.; Hui, D. *Composites, Part B* **2006**, *37*, 437−448.
(21) Park, S.-H.; Yun, D.-J.; Theilmann, P.; Bandaru, P. R. *Polymer* **2013**, *54*, 1318−1322.
(22) Akagi, K.; Tamura, R.; Tsukada, M. *Phys. Rev. Lett.* **1995**, *74* (12), 2307−2310.
(23) Bajpai, V.; Dai, L.; Ohashi, T. *J. Am. Chem. Soc.* **2004**, *126*, 5070.
(24) Pan, L.; Hayashida, T.; Zhang, M.; Nakayama, Y. *Jpn. J. Appl. Phys.* **2001**, *40*, 235−237.
(25) Zhang, Z.; He, P.; Sun, Z.; Feng, T.; Chen, Y.; Li, H.; Tay, B. K. *Appl. Surf. Sci.* **2010**, *256*, 4417−4422.
(26) Volodin, A.; Buntinx, D.; Ahlskog, M.; Fonseca, A.; Nagy, J. v. B.; Van Heasendonck, C. *Nano Lett.* **2004**, *4*, 1775−1779.
(27) Bandaru, P. R.; Rao, A. M. *IEEE Nanotechnology Materials and Devices Conference*, Monterey, CA, Oct 12−15, 2010; Institute of Electrical and Electronics Engineers (IEEE): New York, 2010; pp 113−118.
(28) Tang, N.; Kou, W.; Jeng, C. C.; Wang, L. Y.; Lin, K. J.; Du, Y. W. *ACS Nano* **2010**, *4*, 781−788.
(29) Qi, X.; Zhong, W.; Yao, X. J.; Zhang, H.; Ding, Q.; Wu, Q.; Deng, Y.; Au, C.; Du, Y. W. *Carbon* **2012**, *50*, 646−658.
(30) Fejes, D.; Hernádi, K. *Materials* **2010**, *3*, 2618−2642.
(31) Shaikjee, A.; Coville, N. J. *J. Adv. Res.* **2012**, *3*, 195−223.
(32) Hayashida, T.; Pan, L.; Nakayama, Y. *Physica B* **2002**, *323*, 352−353.
(33) Coluci, V. R.; Fonseca, A. F.; Galvão, D. S.; Daraio, C. *Phys. Rev. Lett.* **2008**, *100*, 086807.
(34) Volodin, A.; Ahlskog, M.; Seynaeve, E.; Van Haesendonck, C.; Fonseca, A.; Nagy, J. B. *Phys. Rev. Lett.* **2000**, *84*, 3342−3345.
(35) Chen, X. Q.; Zhang, S. L.; Dikin, D. A.; Ding, W. Q.; Ruoff, R. S.; Pan, L. J.; Nakayama, Y. *Nano Lett.* **2003**, *3*, 1299−1304.
(36) Poggi, M. A.; Boyles, J. S.; Bottomley, L. A.; McFarland, A. W.; Colton, J. S.; Nguyen, C. V.; Stevens, R. M.; Lillehei, P. T. *Nano Lett.* **2004**, *4*, 1009−1016.
(37) Taiichiro, Y.; Yoshiyuki, S.; Hideto, T.; Hirofumi, T.; Hitoshi, U.; Kazuki, S.; Yoshito, U. *J. Appl. Phys.* **2012**, *112*, 084311.
(38) Stuart, S.; Tutein, A. B.; Harrison, J. A. *J. Chem. Phys.* **2000**, *112*, 6472.
(39) Brenner, D. W.; Shenderova, O. A.; Harrison, J. A.; Stuart, S. J.; Ni, B.; Sinnott, S. B. *J. Phys.: Condens. Matter.* **2002**, *14*, 783.
(40) Shenderova, O. A.; Brenner, D. W.; Omeltchenko, A.; Su, X.; Yang, L. H. *Phys. Rev. B* **2000**, *6*, 61.
(41) Wu, J. Y.; Nagao, S.; He, J. Y.; Zhang, Z. L. *Small* **2013**, DOI: 10.1002/smll.201202830.
(42) Liu, B.; Yu, M. F.; Huang, Y. *Phys. Rev. B* **2004**, *70*, 161402.
(43) Zang, J.; Treibergs, A.; Han, Y.; Liu, F. *Phys. Rev. Lett.* **2004**, *92*, 105501.
(44) López, M. J.; Rubio, A.; Alonso, J. A.; Qin, L. C.; Iijima, S. *Phys. Rev. Lett.* **2001**, *86*, 3056.
(45) Tersoff, J.; Ruoff, R. S. *Phys. Rev. Lett.* **1994**, *73*, 676.
(46) Zhang, R.; Wen, Q.; Qian, W.; Su, D. S.; Zhang, Q.; Wei, F. *Adv. Mater.* **2011**, *30*, 3387.
(47) Shang, Y. Y.; He, X. D.; Li, Y. B.; Zhang, L. H.; Li, Z.; Ji, C. Y.; Shi, E. Z.; Li, P. X.; Zhu, K.; Peng, Q. Y.; Wang, C.; Zhang, X. J.; Wang, R. G.; Wei, J. Q.; Wang, K. L.; Zhu, H. W.; Wu, D. H.; Cao, A. Y. *Adv. Mater.* **2012**, *24*, 2896.
(48) Cao, C. B.; Du, H. L.; Xu, Y. J.; Zhu, H. S.; Zhang, T. H.; Yang, R. *Adv. Mater.* **2008**, *20*, 1738.
(49) Yao, X.; Han, Q. *J. Eng. Mater. Technol.* **2006**, *128*, 419.
(50) Zhang, Y. Y.; Xiang, Y.; Wang, C. M. *J. Appl. Phys.* **2009**, *106*, 113503.
(51) Wang, Y.; Wang, X. X.; Ni, X. G.; Wu, H. A. *Comput. Mater. Sci.* **2005**, *32*, 141.
(52) Yap, H. W.; Lakes, R. S.; Carpick, R. W. *Nano Lett.* **2007**, *7*, 1149.